




Article

Intelligent Fault-Tolerant Control for AC/DC Hybrid Power System of More Electric Aircraft

Lingfei Xiao ^{1,*} , Robert R. Sattarov ² , Peisong Liu ¹  and Cong Lin ¹

¹ College of Energy and Power Engineering, Nanjing University of Aeronautics and Astronautics, Nanjing 210016, China; liupeisong@nuaa.edu.cn (P.L.); lincong@nuaa.edu.cn (C.L.)

² Department of Electromechanics, Ufa State Aviation Technical University, 450025 Ufa, Russia; sattar.rb@gmail.com

* Correspondence: lfxiao@nuaa.edu.cn

Abstract: This paper presents a novel intelligent fault-tolerant control method for a kind of more electric aircraft AC/DC hybrid electrical power system, in order to ensure the safe operation of the engine and improve the power supply quality. The more electric aircraft electrical power system was combined with an aircraft engine, two generators, two AC/DC rectifiers, two DC/AC inverters, DC loads, and AC loads. A multi-objective optimization intelligent sliding mode fault-tolerant controller was obtained for aircraft engine with actuator faults. Each of AC/DC rectifiers is 12-pulse autotransformer rectifier unit with active power filter. Active power filter was used to realize the desired performance of DC bus. Intelligent fractional order PI controller is presented for AC/DC rectifier by considering multiple performance indexes. In order to guarantee the AC-side has satisfying voltage, current, and frequency, no matter the sudden change of AC load that happens or DC/AC fault that occurs, the virtual synchronous generator control method was used for DC/AC inverters. Simulation results verify the effective of the proposed more electric aircraft AC/DC hybrid electrical power system.

Keywords: more electric aircraft; AC/DC hybrid power system; aircraft engine; fault tolerant; grey wolf optimizer; sliding mode



Citation: Xiao, L.; Sattarov, R.R.; Liu, P.; Lin, C. Intelligent Fault-Tolerant Control for AC/DC Hybrid Power System of More Electric Aircraft. *Aerospace* **2022**, *9*, 4. <https://doi.org/10.3390/aerospace9010004>

Academic Editor: Navid Bayati

Received: 20 September 2021

Accepted: 17 December 2021

Published: 22 December 2021

Publisher's Note: MDPI stays neutral with regard to jurisdictional claims in published maps and institutional affiliations.



Copyright: © 2021 by the authors. Licensee MDPI, Basel, Switzerland. This article is an open access article distributed under the terms and conditions of the Creative Commons Attribution (CC BY) license (<https://creativecommons.org/licenses/by/4.0/>).

1. Introduction

In conventional aircrafts, secondary energy sources include hydraulic, pneumatic, and electrical energy. Since the 1970s, more electric aircraft (MEA) has been developed. The main concept of MEA is to replace most of secondary energy with electrical energy when driving aircraft subsystems [1,2]. Therefore, the demand for electrical energy of MEA is greatly increased compared with traditional aircraft. For example, B787 with multiple generators has a generating capacity to the level of megawatt (MW) to provide electric power for electrical equipment onboard [3,4].

The B787, A380, and F35 are the three typical types of MEA, which use different power systems. B787 and A380 generate electricity through variable frequency alternating current (AC) generators, of which B787 generates 235 V 400 Hz AC and obtains 270 V direct current (DC) by power electronic converters, leading to a hybrid AC/DC power supply system. However, F35 directly uses DC generators to produce 270 V DC as the main power supply [5,6].

Usually, for large manned aircrafts, their energy comes from burning fuel by aircraft engines. In MEA, most of the energy is used to provide aircraft thrust. However, more and more electrical power is drawn from aircraft engines by generators with the increment of electrical power requirement in MEA, and the stability of aircraft engines is important for the performance of electrical power. Therefore, it is necessary to design suitable control methods for MEA electrical power system including aircraft engines.

Recently, some scholars have studied the integrated control of engine propulsion and electrical power. Reference [7] gave an overview of their studies of electrical power

management solutions based on an integrated engine/power control system for MEA and proposed a power control concept based on integrated engine control technologies that ensure stable power systems. Reference [8] developed a rate-based model predictive controller for handling large power load transients through coordination of the engine and hybrid power subsystems in an aircraft.

Meanwhile, there are many investigations that are carried out on the control problems of different components in MEA power systems, conventional aircraft power systems, and common electrical power systems. In order to meet the performance optimization requirements in aircraft engines, Reference [9] presented a non-linear model predictive control method based on elastic back propagation (BP) neural network with hybrid grey wolf optimizer (GWO). On the basis of adaptive observer, Reference [10] proposed a fault-tolerant control (FTC) method for aircraft engines with sensor faults and actuator faults. Reference [11] used the method of decoupling start control for aircraft wound-rotor synchronous starter-generator and achieved good results. Reference [12] established a model of high-voltage direct current (HVDC) power generation system and proposed a double closed-loop feedback voltage regulator technology in MEA. Reference [13] discussed the stability of hybrid AC/DC power systems for MEA. [14] proposed a new adaptive sliding manifold design method and addressed a bidirectional voltage converter of MEA. Reference [15] designed a supervisor to select the appropriate controller for each control task of the basic general electrical aircraft architecture by controlling the bidirectional converter. Reference [16] provided an active filtering scheme for the AC/DC hybrid power system of MEA, which improves the reliability of the power system. Reference [17] proposed an induction generator power supply scheme for the AC/DC hybrid power system. Reference [18] presented a comprehensive control design procedure for AC/DC converters and DC/AC inverters based on sliding mode control (SMC) method. Reference [19] gave an unified control strategy for inverter-based micro-grid using hybrid droop scheme. Reference [20] studied enhanced virtual synchronous generator (VSG) control for parallel inverters in micro-grids.

Moreover, intelligent control has attracted lots of attentions on various of areas recently, including MEA power systems. Intelligent control is a type of method that can achieve control target with as little human intervention as possible, including fuzzy control, neural network control, and meta-heuristic optimization techniques for control systems [9,21,22]. An intelligent power allocation and load management method of MEA was proposed in [23]. Reference [24] used an adaptive tabu search algorithm and neural network to control the active power filter (APF) in MEA, making the AC power frequency be 400Hz.

Moreover, with the increasing complexity of modern engineering systems, the possibility of occurring faults increases as well. The traditional robust controllers, which are designed to deal with uncertainties, may fail or at least provide reduced performance, when the systems suffer from faults. Therefore, in order to maintain stability and acceptable performance for faulty systems, FTC has been studied by more and more researchers. Based on the sliding mode theory, Reference [25] presented a robust FTC for aircraft engine with faults via adaptive faults diagnosis. Reference [26] proposed an adaptive passive FTC method for actuator faults of affine class of multi-input multi-output non-linear systems with uncertainties using SMC. Reference [27] illustrated an energy-efficient power management solution for a fault-tolerant more electric engine/aircraft.

Therefore, the purpose of this paper is to present a AC/DC hybrid power system for MEA and the corresponding intelligent FTC method, to ensure the safe operation of the engine, improve the power supply quality, and achieve multi-objective optimization of the system.

The main contributions of this paper include:

- (1) A novel AC/DC hybrid electrical power system for MEA is designed;
- (2) A multi-objective optimization intelligent sliding mode fault-tolerant control (SMFTC) law is constructed for aircraft engine with actuator faults;

- (3) In order to realize the DC bus has desired performance, active power filter is combined with autotransformer rectifier unit (APF-ATRU). Intelligent fractional order PI (FOPI) controller is presented for the APF-ATRU by considering multiple performance indexes;
- (4) VSG is used for DC/AC to guarantee the AC-side has satisfying voltage, current, and frequency, no matter what sudden change of AC load happens or DC/AC fault occurs.

The remainder of this paper is organized as follows: Section 2 shows the composition of the MEA AC/DC hybrid electrical power system in this paper. Section 3 presents the intelligent FTC for DC bus power supply-side, including intelligent FTC for aircraft engine, control for generators, and intelligent control for AC/DC rectifiers. Section 4 gives the DC/AC control design based on VSG. Simulation on the whole MEA power control system is shown in Section 5, in order to verify the effect of the presented intelligent FTC method. Section 6 draws the conclusions of this paper.

2. More Electric Aircraft AC/DC Hybrid Electrical Power System Design

In addition to providing the power required for aircraft flight, an aircraft engine also provides power for the secondary power systems on the aircraft. As various types of airborne equipment of aircraft consume more and more electrical energy, the demand for aircraft electrical power is also greater. In the past few decades, with the rapid development of power electronic technology, the concept of more electric has appeared in modern aircrafts [28]. Figure 1 shows the power system with the electrical power about 1.5 MW on a MEA.

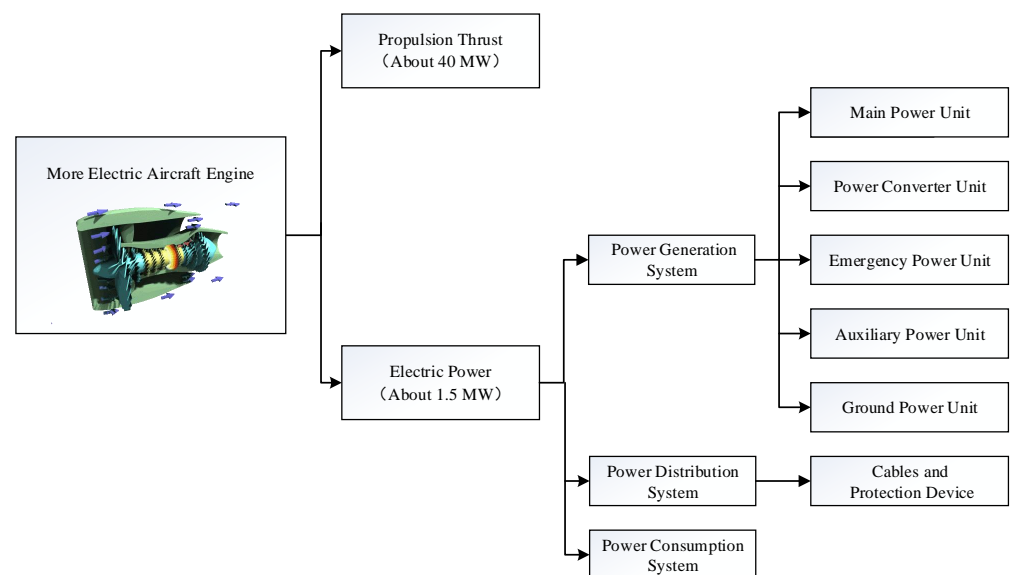


Figure 1. Power system on a more electric aircraft.

With the increasing demand in aircraft electricity, the power generation capacity has increased significantly. In order to improve the efficiency of electrical power generation and reduce various losses of the power generation system, the voltage level increases continuously. Compared with the traditional power supply system, the 270 V DC power supply system has the advantages of higher power generation efficiency, lighter weight of the electrical power generation and distribution system, easier to achieve uninterrupted power supply, and higher reliability. Hence, a 270 V DC power supply system is very promising.

However, there are not only DC loads but also AC loads on MEA. For the loads, the normal working voltage must not deviate too much from the rated voltage. When voltage changes greatly, some control methods are needed to keep voltage stable.

Moreover, due to uncertainties and faults in the aircraft engine, and the diversity and variability of electrical loads, fluctuation in the DC bus voltage may be significant. The unstable engines, generators, rectifiers, inverters, and so on may cause serious safety hazards.

Therefore, the purpose of this section is to present a novel MEA AC/DC hybrid power system and the corresponding control strategy.

In light of Boeing 787, each aircraft engine drives two AC generators in parallel. Therefore, the following MEA AC/DC hybrid electrical power system with 270 V DC Bus and 115 V 400 Hz AC Bus are designed.

As shown in Figure 2, the rated voltage of the DC bus is 270 V, the rated voltage of the AC bus is 115 V, and the frequency is 400 Hz.

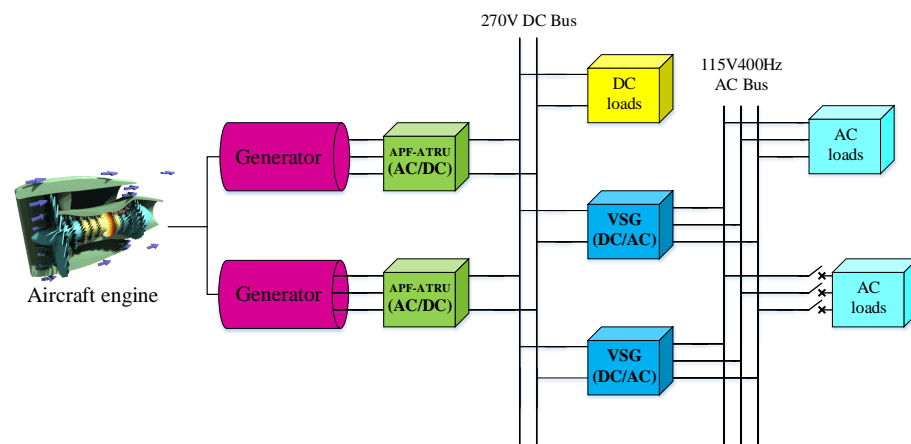


Figure 2. MEA AC/DC hybrid electrical power system.

The DC bus and its user-side equipment constitute the electrical load for the DC bus power supply-side equipment.

The DC bus power supply-side is composed of an aircraft engine, two generators, and two AC/DC rectifiers. The AC/DC rectifiers are of APF-ATRU. They are used to rectify the variable frequency AC output from the generators to 270 V DC output. The APF-ATRU method is used to improve the input current quality of AC/DC and is beneficial for reducing the volume and weight of AC/DC.

The user-side of the DC bus consists of a DC load, two DC/AC converters, a 115 V 400 Hz AC bus, and two AC loads. The function of DC/AC is to invert 270 V DC to 115 V 400 Hz AC output. VSG control technology is used for the two DC/AC inverters. Two DC/AC converters help to guarantee the MEA power system has fault-tolerant ability once one of the DC/AC converters fails.

With the increase in power consumption of airborne equipment, sometimes multiple power electronic converters are required to work in parallel, and there are many reasons for parallel operation of inverters. Firstly, the number of high-current power electronic devices is limited. Secondly, the parallel operation of the inverters can provide the power supply system with redundancy and the high reliability required for critical onboard equipment. Thirdly, the parallel operation of inverters can also reduce the heat generation of high-power inverters. Therefore, multiple inverters connected in parallel in the presented DC/AC hybrid power system improve the power transmission efficiency and the reliability of the power supply system.

Compared with the traditional DC/AC converter control scheme, the scheme of using multiple VSGs in parallel converts 270 V DC to 115 V 400 Hz AC and can simulate the characteristics of synchronous generator active frequency regulation and reactive power voltage regulation through the VSG control algorithm, so as to ensure the stability of the power system.

Therefore, the presented MEA AC/DC hybrid power system can meet the demand for electrical energy and safe operation of engine, while taking into account the diversity of electrical equipment on MEA.

3. Intelligent Fault-Tolerant Control for DC Bus Power Supply-Side

According to Figure 2, the DC bus power supply-side is comprised of aircraft engine, generators, and AC/DC rectifiers. In the following, aircraft engine intelligent FTC is studied at first, and then PI control for generators and intelligent FOPI control for AC/DC rectifiers are given.

3.1. Intelligent Fault-Tolerant Control for Aircraft Engine

FTC can adjust system components during operation when faults occur and maintain the stability of the systems under acceptable conditions. Because of the important role in keeping safety, FTC has attracted extensive attention from industry, including the aviation industry [29,30].

Aircraft engines often suffer harsh working environments, such as high temperature, high pressure, and high vibration. It is inevitable that uncertainties happen and faults in actuators may occur. Therefore, studying robust FTC methods for aircraft engines is necessary.

Meanwhile, the two generators are usually connected to the low-pressure spool of engine. Thus, the steady-state and dynamics of the low-pressure spool speed of aircraft engine are important in the MEA power system.

Moreover, amongst several types of faults, actuator faults are the most important, because they affect the behavior of system directly.

Hence, in the following subsection, due to the advantage of SMC method in handling uncertainties, an intelligent SMFTC for aircraft engine is designed, in order to realize that the states of aircraft engine are stable robustly while the actuator faults occur.

3.1.1. The Uncertain Linear Dynamic Model of Aircraft Engine with Actuator Faults

Aircraft engine is distinguished by its highly complicated and non-linear, and can be represented as

$$\dot{\mathbf{x}} = \mathbf{f}(\mathbf{x}, \mathbf{u}) \quad (1a)$$

$$\mathbf{y} = \mathbf{g}(\mathbf{x}, \mathbf{u}) \quad (1b)$$

where $\mathbf{x} = [x_1, x_2, \dots, x_n]^T \in \mathbf{R}^n$ is the state vector, $\mathbf{u} = [u_1, u_2, \dots, u_m]^T \in \mathbf{R}^m$ is the input vector, and $\mathbf{y} = [y_1, y_2, \dots, y_r]^T \in \mathbf{R}^r$ is the output vector, with n, m, r being the dimensions of state, input, and output, respectively. \mathbf{f} and \mathbf{g} are non-linear functions.

For a twin-shaft aircraft engine, the state vector \mathbf{x} can include low-pressure spool speed n_l and high-pressure spool speed n_h ; the control vector \mathbf{u} may contain the main fuel flow W_{fb} , nozzle throat area A_8 ; the output vector \mathbf{y} can be comprised of low-pressure spool speed n_l , total temperature of low-pressure turbine T_5 [25].

However, a too complex dynamic model of aircraft engine should be avoided in designing control law, so that the computational burden can be not heavy and meet the real-time requirement as a result. Therefore, the linearized aircraft engine dynamic model is employed usually, especially when the aircraft engine works at a certain operation point, such as rated operating point, cruise operating point, and so on.

The model (2) is the typical linear state space model of an aircraft engine, while the aircraft engine works at a certain operation point—take rated operating point as an example.

$$\delta\dot{\mathbf{x}} = A\delta\mathbf{x} + B\delta\mathbf{u} \quad (2a)$$

$$\delta\mathbf{y} = C\delta\mathbf{x} + D\delta\mathbf{u} \quad (2b)$$

where δx , δy , and δu are the normalized deviation state vector, normalized deviation output vector, and normalized deviation input vector, respectively. Namely,

$$\delta x = \begin{bmatrix} \delta x_1 \\ \delta x_2 \\ \vdots \\ \delta x_n \end{bmatrix} = \begin{bmatrix} \frac{x_1 - x_{10}}{x_{10}} \\ \frac{x_2 - x_{20}}{x_{20}} \\ \vdots \\ \frac{x_n - x_{n0}}{x_{n0}} \end{bmatrix}, \quad \delta y = \begin{bmatrix} \delta y_1 \\ \delta y_2 \\ \vdots \\ \delta y_r \end{bmatrix} = \begin{bmatrix} \frac{y_1 - y_{10}}{y_{10}} \\ \frac{y_2 - y_{20}}{y_{20}} \\ \vdots \\ \frac{y_r - y_{r0}}{y_{r0}} \end{bmatrix}, \quad \delta u = \begin{bmatrix} \delta u_1 \\ \delta u_2 \\ \vdots \\ \delta u_m \end{bmatrix} = \begin{bmatrix} \frac{u_1 - u_{10}}{u_{10}} \\ \frac{u_2 - u_{20}}{u_{20}} \\ \vdots \\ \frac{u_m - u_{m0}}{u_{m0}} \end{bmatrix}$$

with $x_0 = [x_{10}, x_{20}, \dots, x_{n0}]^T$, $y_0 = [y_{10}, y_{20}, \dots, y_{r0}]^T$, and $u_0 = [u_{10}, u_{20}, \dots, u_{m0}]^T$ being the steady-state vector, steady-output vector, and steady-input vector of the certain operating point, respectively. A, B, C, D are matrices of appropriate dimensions; they can be obtained by the fitting method or system identification [31,32], according to the non-linear model of the aircraft engine (1) works at the considered operation point. For a normal running aircraft engine, the matrix A should be Hurwitz, and it is assumed that (A, B) is controllable.

Considering a twin-shaft aircraft engine, it is suitable to choose

$$\delta x = \begin{bmatrix} \frac{n_h - n_{h0}}{n_{h0}} \\ \frac{n_l - n_{l0}}{n_{l0}} \end{bmatrix} \triangleq \begin{bmatrix} \delta n_h \\ \delta n_l \end{bmatrix}, \quad \delta y = \begin{bmatrix} \frac{n_l - n_{l0}}{T_5 - T_{50}} \\ T_5 \end{bmatrix} \triangleq \begin{bmatrix} \delta n_l \\ \delta T_5 \end{bmatrix}, \quad \delta u = \begin{bmatrix} \frac{W_{fb} - W_{fb0}}{W_{fb0}} \\ \frac{A_8 - A_{80}}{A_{80}} \end{bmatrix} \triangleq \begin{bmatrix} \delta W_{fb} \\ \delta A_8 \end{bmatrix}$$

where $n_{h0}, n_{l0}, W_{fb0}, A_{80}, T_{50}$ are the steady values of high-pressure spool speed n_h , low-pressure spool speed n_l , total temperature of low-pressure turbine T_5 , main fuel flow W_{fb} , and nozzle throat area A_8 at the certain operating point, respectively. Then, (2) is expressed as

$$\begin{aligned} \begin{bmatrix} \delta \dot{n}_h \\ \delta \dot{n}_l \end{bmatrix} &= \begin{bmatrix} a_{11} & a_{12} \\ a_{21} & a_{22} \end{bmatrix} \begin{bmatrix} \delta n_h \\ \delta n_l \end{bmatrix} + \begin{bmatrix} b_{11} & b_{12} \\ b_{21} & b_{22} \end{bmatrix} \begin{bmatrix} \delta W_{fb} \\ \delta A_8 \end{bmatrix} \\ \begin{bmatrix} \delta n_l \\ \delta T_5 \end{bmatrix} &= \begin{bmatrix} 0 & 1 \\ c_{21} & c_{22} \end{bmatrix} \begin{bmatrix} \delta n_h \\ \delta n_l \end{bmatrix} + \begin{bmatrix} 0 & 0 \\ d_{21} & d_{22} \end{bmatrix} \begin{bmatrix} \delta W_{fb} \\ \delta A_8 \end{bmatrix} \end{aligned} \tag{3}$$

where $a_{11}, a_{12}, a_{21}, a_{22}$ are elements in matrix A , $b_{11}, b_{12}, b_{21}, b_{22}$ are elements in matrix B , c_{21}, c_{22} are elements in matrix C , and d_{21}, d_{22} are elements in matrix D . Clearly, δT_5 is related to $\delta n_h, \delta n_l$ by matrix C .

The following work focuses on a twin-shaft aircraft engine working around a certain operation point, whose linear dynamic model is described as (3). For the ease of expression, the symbol δ in (2) is ignored, and then (2) is rewritten as (4),

$$\dot{x} = Ax + Bu \tag{4a}$$

$$y = Cx + Du \tag{4b}$$

Because of the non-linearity of aircraft engine, manufacturing tolerances, aircraft engine aging, and some disturbances in flight, the effect of unmodelled non-linear dynamics, parameter uncertainties, external disturbances, and so on should be considered into the dynamic model of aircraft engine. Thus, the uncertain linear dynamic model of aircraft engine can be described by

$$\dot{x} = Ax + Bu + \eta \tag{5}$$

where $\eta = [\eta_1, \eta_2]^T$ is lumped disturbance, including unmodelled non-linear dynamics, parameter uncertainties, external disturbances, and so on.

In (5), because η is lumped disturbance, it may depend on the state x . Usually, to ensure the safety of aircraft engine, its operation is limited to a bounded area [31,32].

Figure 3 shows an engine operating line and various constraints represented on a compressor map. In Figure 3, the engine operating line is the locus of compressor pressure

ratio and mass flow rate points obtained at steady-state conditions as an engine input is varied. Obviously, there are idle limit, maximum speed limit, turbine temperature limit, and so on. Because speeds are selected to be the state x , the state is bounded. A more detailed illustration can be found in [32].

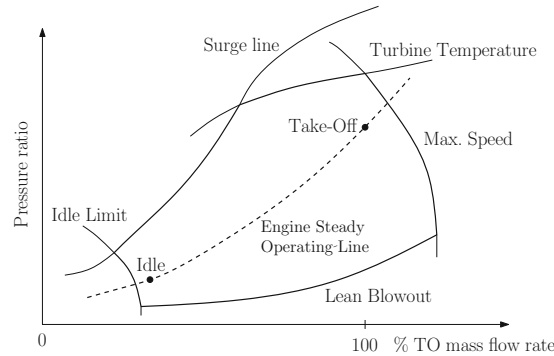


Figure 3. Engine line and operating limits on compressor map [32].

Thus, it is suitable to assume that x is limited, the initial value x_0 is bounded in a subset of R^2 , and the boundaries of η_1, η_2 are known as $\bar{\eta}_1, \bar{\eta}_2$, with $\bar{\eta}_1 > 0$ and $\bar{\eta}_2 > 0$, respectively.

Considering the possible faults in actuators, on the basis of (5), gives

$$\dot{x} = Ax + B\rho u_0 + \eta \tag{6}$$

where $u = \rho u_0$, u_0 is the control signal vector carried on actuators, $\rho = \text{diag}\{\rho_1, \rho_2\}$ is the matrix of fault coefficient, with $0 < \rho_1 \leq 1, 0 < \rho_2 \leq 1$. When $\rho_i, (i = 1, 2)$ is zero, it means the corresponding actuator fails totally, and when ρ_i is equal to one, it means the fault does not occur in the corresponding actuator. For the case of $\rho_i, (i = 1, 2)$ is zero, it is out of the range of this paper, that is, the actuators are with partial failure or without fault.

3.1.2. Sliding Mode Fault-Tolerant Controller Design

SMC method is one of the widespread robust control methods: its principle is simple, and two steps are needed to complete the control system design. The first step is to specify a sliding mode surface with the desired steady-state and dynamic performance, while the second step is to construct a suitable controller to force the states of system to reach the sliding mode surface and keep on it thereafter [33]. Therefore, in the following subsection, an integral sliding mode surface is designed at first, and then, the sliding mode controller is obtained according to reaching law approach.

Define a sliding mode function as

$$s = x + \sigma \int_0^t x d\tau \tag{7}$$

where $s = [s_1, s_2]^T$ is sliding mode variable vector, $\sigma = \text{diag}\{\sigma_1, \sigma_2\}$ is positive matrix. σ is the designable parameter matrix and is used to guarantee the stability of sliding mode surface $S = \{x | s(x) = 0\}$.

Here, the reaching law approach is used to realize that the states reach sliding mode surface and then remain on it, namely, to meet the reaching condition $s^T \dot{s} < 0$.

The following constant plus proportional rate reaching law is employed,

$$\dot{s} = -qs - k\text{sgn}(s) \tag{8}$$

where $\text{sgn}(s) = [\text{sgn}(s_1), \text{sgn}(s_2)]^T$, with $\text{sgn}(\cdot)$ being a sign function. $q = \text{diag}\{q_1, q_2\}$, $k = \text{diag}\{k_1, k_2\}$ are a positive designable matrix. It is assumed that $k_1 > \bar{\eta}_1, k_2 > \bar{\eta}_2$.

Deriving (7) gives

$$\dot{s} = \dot{x} + \sigma x \quad (9)$$

Considering the nominal model of aircraft engine (4) and substituting (4a) into (9) yields

$$\dot{s} = Ax + Bu + \sigma x \quad (10)$$

Compare (10) with (8), it gives

$$Ax + Bu + \sigma x = -qs - k\text{sgn}(s)$$

Thus, the control signal u_0 is obtained as follows:

$$u_0 = -(B\rho)^{-1}[qs + k\text{sgn}(s) + Ax + \sigma x] \quad (11)$$

where the inverse matrix of $B\rho$ is required. In case $B\rho$ is not invertible, the pseudo inverse of $B\rho$ is used to replace its inverse matrix.

Substituting (11) into (7) and considering the uncertain model of aircraft engine (6) gives

$$\begin{aligned} \dot{s} &= Ax + B\rho u_0 + \eta + \sigma x \\ &= Ax - [qs + k\text{sgn}(s) + Ax + \sigma x] + \eta + \sigma x \\ &= -qs - k\text{sgn}(s) + \eta \end{aligned}$$

By selecting the Lyapunov function as $V = \frac{1}{2}s^T s$, the derivative of V is

$$\begin{aligned} \dot{V} &= s^T \dot{s} \\ &= s^T [-qs - k\text{sgn}(s) + \eta] \end{aligned}$$

Obviously, when $k_1 > \bar{\eta}_1$, $k_2 > \bar{\eta}_2$, there exists $\dot{V} < 0$, namely, the reaching condition $s^T \dot{s} < 0$ is held. Therefore, the sliding mode surface (7) can be reached, and the states of aircraft engine can be stable robustly with the controller (11).

3.1.3. Intelligent Optimization for Sliding Mode Fault-Tolerant Controller

Generally, the state deviation from the equilibrium point is expected to be as small as possible, and the minimizing of input energy consumption is expected as well. Therefore, the multi-objective performance indexes for the aircraft engine are

$$J_1 = \int_0^t x^T x d\tau \quad (12a)$$

$$J_2 = \int_0^t u^T u d\tau \quad (12b)$$

where J_1 describes steady-state control precision requirement, and J_2 shows the attention on input energy consumption.

In the following subsection, GWO is used to realize the multi-objective optimization for aircraft engine by searching the optimal control designable parameters in (11).

In [21], the principle of GWO was given. GWO is a kind of meta-heuristic optimization algorithm, which is inspired by the primary phases of grey wolf hunting. Grey wolves hunt prey in group with three main phases: searching, encircling, and attacking.

Usually, from five to twelve wolves live in a group with very strict social dominant hierarchy. The hierarchy has four levels, from the top level to the bottom level, the wolves are called alpha wolves (α_{GWO}), beta wolves (β_{GWO}), delta wolves (δ_{GWO}), and omega wolves (ω_{GWO}), respectively. Accordingly, in the mathematical model of GWO, the fittest solution is the α_{GWO} , and the second and third best solutions are named β_{GWO} and δ_{GWO} , respectively. The rest of the candidate solutions are assumed to be ω_{GWO} .

The optimization imitates the hunting process of grey wolves and starts by creating a random population of grey wolves. When the maximum number of iterations is reached, α_{GWO} , β_{GWO} , and δ_{GWO} wolves estimate the probable position of the prey.

The main mathematical equations of describing the hunting process are:

$$\begin{aligned}\vec{X}(t_{GWO} + 1) &= \vec{X}_p(t_{GWO}) - \vec{A}\vec{D} \\ \vec{A} &= 2\vec{a}\vec{r}_1 - \vec{a}, \quad \vec{C} = 2\vec{r}_2, \quad \vec{D} = |\vec{C}\vec{X}_p(t_{GWO}) - \vec{X}(t_{GWO})|\end{aligned}\quad (13)$$

where t_{GWO} is the current iteration, $\vec{X}_p(t_{GWO})$ and $\vec{X}(t_{GWO})$ are the position vector of the prey and a grey wolf, respectively. \vec{A} and \vec{C} are coefficient vectors, \vec{a} is linearly decreased from 2 to 0 in the course of iterations, and \vec{r}_1 and \vec{r}_2 are random vectors in $[0, 1]$. \vec{D} is an intermediate auxiliary variable.

In GWO, it is assumed that the α_{GWO} (best candidate solution), β_{GWO} , and δ_{GWO} have better knowledge about the possible location of prey. GWO saves the first three best solutions obtained at current iteration and obliges other search agents (including ω_{GWO}) to update their positions on the basis of the position of the best search agents. That is, α_{GWO} , β_{GWO} , and δ_{GWO} estimate the position of the prey, while the other wolves update their positions around the prey randomly. Based on (13), (14) are used to describe this behavior.

$$\begin{aligned}\vec{D}_\alpha &= |\vec{C}_1\vec{X}_\alpha - \vec{X}|, \quad \vec{D}_\beta = |\vec{C}_2\vec{X}_\beta - \vec{X}|, \quad \vec{D}_\delta = |\vec{C}_3\vec{X}_\delta - \vec{X}|, \\ \vec{X}_1 &= \vec{X}_\alpha - \vec{A}_1\vec{D}_\alpha, \quad \vec{X}_2 = \vec{X}_\beta - \vec{A}_2\vec{D}_\beta, \quad \vec{X}_3 = \vec{X}_\delta - \vec{A}_3\vec{D}_\delta, \\ \vec{X}(t_{GWO} + 1) &= \frac{\vec{X}_1 + \vec{X}_2 + \vec{X}_3}{3}\end{aligned}\quad (14)$$

where the subscripts $(\cdot)_\alpha$, $(\cdot)_\beta$, and $(\cdot)_\delta$ are with respect to the α_{GWO} , β_{GWO} , and δ_{GWO} grey wolves, respectively. \vec{X}_1 , \vec{X}_2 , and \vec{X}_3 are intermediate auxiliary variables.

The optimal costs and the corresponding position of wolves are put into archive in each iteration, according to the performance index of wolves. The GWO terminate once the maximum number of iterations is arrived, and then GWO returns a group of non-dominated solutions.

According to the SMC theory [33], σ , q , and k are crucial for the steady-state and dynamic control performance of aircraft engine. Moreover, it is clear that k should be large enough to deal with the influence of lumped disturbance. However, large k increases the value of control signal, as shown in the control law (11). Thus, σ_1 , σ_2 , q_1 , q_2 , k_1 , and k_2 are key parameters in controller for obtaining the minimum performance indexes (12).

Therefore, when GWO is used to realize aircraft engine intelligent SMFTC, the $\vec{X}(t_{GWO})$ described by (13) for each t_{GWO} is $\vec{X} = [\sigma_1, \sigma_2, q_1, q_2, k_1, k_2]$.

The block diagram of the proposed intelligent SMFTC method for aircraft engine is shown in Figure 4.

Remark 1. Usually, the linear quadratic regulation (LQR) performance index is

$$J = \int_0^t (x^T Q x + u^T R u) d\tau \quad (15)$$

where x is state, u is input, and Q, R are weighted matrices.

Clearly, the performance indexes in (12) are J_1 and J_2 . LQR performance index (15) is a combination of J_1 and J_2 by fixed weighted matrices Q and R . Thus, the optimization in this paper is not limited by specifying certain weighted matrices Q and R .

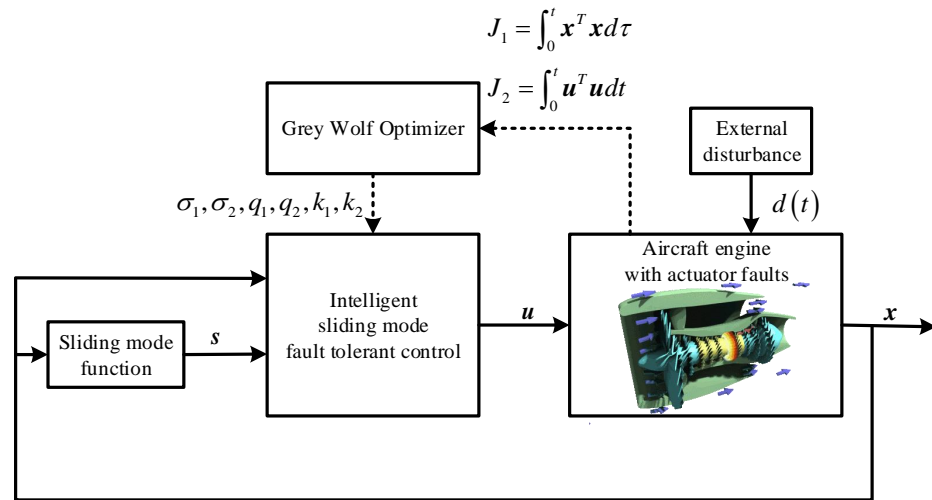


Figure 4. The block diagram of intelligent sliding mode fault-tolerant control method for aircraft engine.

3.2. Control for Generators

Considering the generators are driven by the low-pressure spool of aircraft engine directly, the speed of generators is the same as that of the low-pressure spool in aircraft engine.

The voltage regulator is one of the ways to maintain the voltage stability of the power supply system. Its basic principle is to achieve the purpose of controlling the generator output voltage by adjusting the excitation current. Its main functions include:

- Adjusting the excitation current of the alternator such that the generator output voltage does not change due to the changes of load or speed;
- Limiting the maximum value of generator phase voltage.

Here, PI controller is designed for the two generators.

The PI controller, whose transfer function can be expressed as

$$G_{cG}(s) = k_{pG} + k_{iG} \frac{1}{s} \tag{16}$$

where k_{pG} and k_{iG} are proportional coefficient and integral coefficient, respectively. s is Laplace operator.

The block diagram of PI control for a generator is shown in Figure 5.

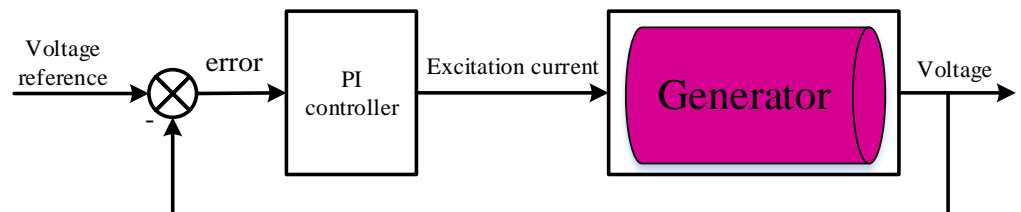


Figure 5. The block diagram of intelligent control for a generator.

3.3. Intelligent Control for AC/DC Rectifiers

3.3.1. Control for AC/DC Rectifiers

Power electronics is important for the MEA [28]. Power electronic converters are divided into four types: AC/DC rectifier, DC/DC converter, DC/AC inverter, and AC/AC transformer. Among them, AC/DC converters refer to the multi-pulse rectification technology, and the three-phase bridges are commonly used rectifier circuits.

Because the weight and volume are increased with the number of pulses in autotransformer rectifiers, a 12-pulse autotransformer rectifier unit (ATRU) is applied in this paper.

The variability of electrical loads results in a fluctuation in the DC bus voltage. In order to reduce the fluctuation, APF is used to improve the performance of ATRU.

Figure 6 shows the design of 12-pulse ATRU with APF; the DC-side parallel APF topology diagram is shown in Figure 7; Figure 8 shows the equivalent circuit diagram of the DC-side APF; and Figure 9 gives the control scheme for APF-ATRU.

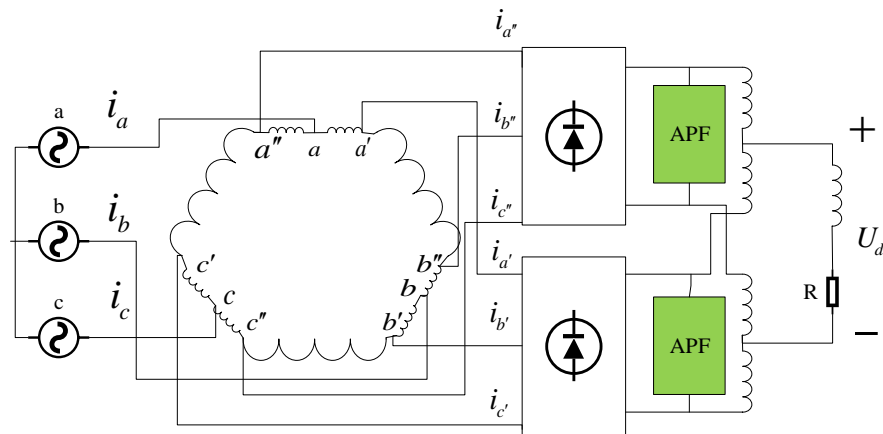


Figure 6. 12-pulse autotransformer rectifier unit with active power filter.

It can be seen from Figure 6 that this topology is based on a 12-pulse ATRU, and two parallel APFs are in the output of the three-phase uncontrolled rectifier bridge. Since the input voltages of the two sets of three-phase uncontrolled rectifier bridges have phase difference, their output instantaneous voltages are not equal. In order to ensure normal operation, balanced reactors are used to smooth the two sets of DC voltage, so that the total output voltage meets the working conditions.

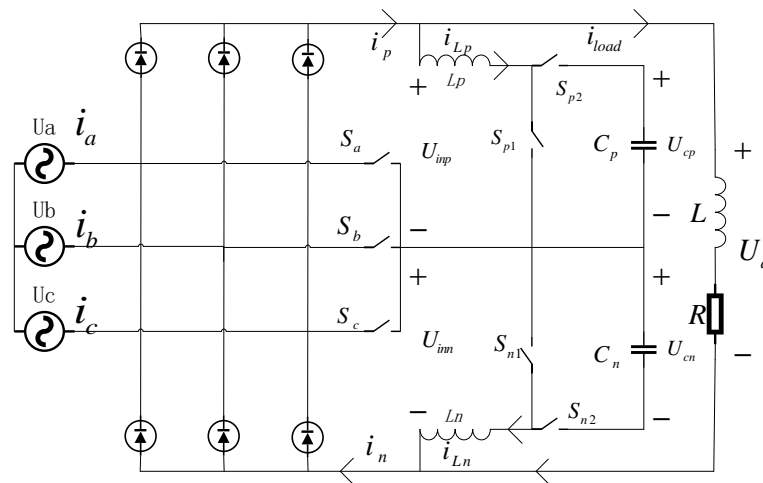


Figure 7. DC-side parallel APF topology diagram.

Because the 12-pulse ATRU based on DC-side parallel APF designed in this paper is composed of two three-phase bridges, in order to describe the problem conveniently, here, a three-phase bridge is shown in Figure 7 as an example to introduce.

In Figure 7, L_p , S_{p1} , S_{p2} , C_p and L_n , S_{n1} , S_{n2} , C_n , constitute a bidirectional dual boost circuit, together with a low-frequency bidirectional switch S_a , S_b , S_c constitute a main circuit of a DC-side parallel APF, where L_p and L_n are filter inductors. S_{p1} , S_{p2} , S_{n1} , S_{n2} are high-frequency switches, C_p and C_n capacitances. The low-frequency switches work at double the fundamental frequency, while the S_{p1} , S_{p2} , S_{n1} , and S_{n2} work at high frequency, and the two pairs of high-frequency switches work complementary to each other. The three low-frequency switches are only turned on one at a time, and the conduction rule is that the

one at the intermediate voltage is turned on. Compared with low-frequency switching, the frequency of high-frequency switching is very high; therefore, a certain voltage conduction can be used as an example for illustration.

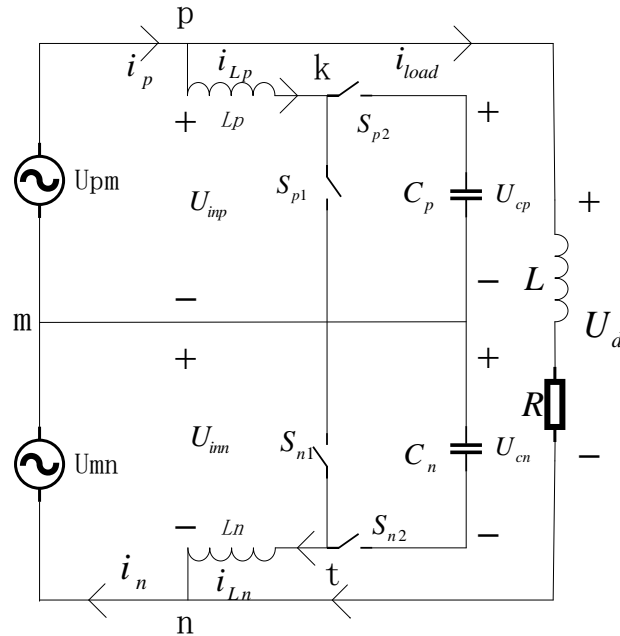


Figure 8. Equivalent circuit diagram of DC-side APF.

As shown in the equivalent circuit diagram of DC-side APF, i.e., Figure 8, when S_{p1} and S_{p2} are closed, the filter inductor is directly connected to the power supply. At this time, the power supply charges the filter inductor, namely, the inductor current increases, giving

$$U_{Lp} = U_{pm} = L \frac{di_{Lp}}{dt} > 0 \tag{17a}$$

$$U_{Ln} = U_{mn} = L \frac{di_{Ln}}{dt} > 0 \tag{17b}$$

where U_{Lp} , U_{Ln} are the voltages of L_p and L_n , respectively. Moreover, U_{pm} is the voltage between point p and m , and U_{mn} is the voltage between point m and n .

When S_{p2} and S_{n2} are closed, the voltage across the filter inductor can be expressed as:

$$U_{Lp} = U_{pm} - U_{Cp} = L \frac{di_{Lp}}{dt} < 0 \tag{18a}$$

$$U_{Ln} = U_{mn} - U_{Cn} = L \frac{di_{Ln}}{dt} < 0 \tag{18b}$$

U_{Cp} and U_{Cn} are the voltages of C_p and C_n , respectively; i_{Lp} and i_{Ln} are the currents through L_p and L_n , respectively.

It can be seen that the voltage across the inductor decreases, that is, the inductor current decreases. Similarly, when S_{p1} and S_{n2} are closed or when S_{p2} and S_{n1} are closed, the voltage across the two filter inductors increases or decreases accordingly.

From the above analysis, it can be seen that the voltage across the filter inductor can be positive or negative, and thus the inductor current can be increased or decreased, which means the current is controllable. Therefore, when proper control is applied, the circuit can be viewed as a controlled current source, thereby achieving compensation for the harmonic current of the non-linear load.

The dual-loop control scheme is used for the control of APF-ATRU. A FOPI voltage controller for the outer loop and PI current controller for the inner loop. Moreover, the

multi-objective optimization algorithm based on GWO is used to optimize the control system. Figure 9 shows the schematic diagram of the control for APF-ATRU. According to Figure 9, GWO is used to tuning the parameters of FOPI controller, while GWO is on the basis of minimizing two performance indexes for APF-ATRU. The two performance indexes are the integral of time and absolute error (ITAE) and the total harmonic distortion (THD), respectively.

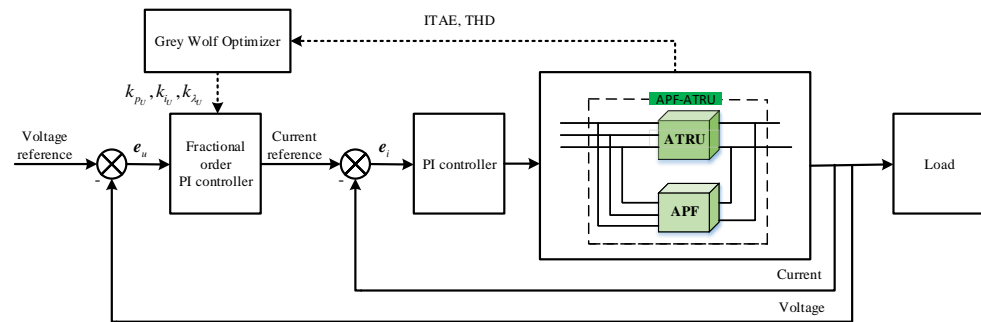


Figure 9. Intelligent control for APF-ATRU.

The voltage controller in outer loop is to ensure stability of voltage and provide the reference signal for the current controller. The transfer function of FOPI controller can be expressed as

$$G_{cU}(s) = k_{pU} + k_{iU}s^{k_{\lambda U}} \tag{19}$$

where k_{pU} and k_{iU} are proportional coefficient and integral coefficient, respectively. k_{pU} , k_{iU} , and $k_{\lambda U}$ are the designable parameters in FOPI controller, and they are optimized by GWO, as shown in Figure 9. Compared with PI controller of integer order, PI controller of fractional order increases the integral order $k_{\lambda U}$.

The current controller in inner loop is to ensure that the DC-side APF can compensate the DC-side current in real time. PI controller is designed for the inner loop, with k_{pI} and k_{iI} being the designable parameters in the controller.

According to Figure 2, there are two AC/DCs, it is supposed that the same FOPI controller parameters k_{pU} , k_{iU} and $k_{\lambda U}$ in voltage outer loop, and the same PI controller parameters k_{pI} , k_{iI} in current inner loop are used in each APF.

3.3.2. Intelligent Optimization for Controller Parameters in AC/DC Rectifiers

In the following subsection, GWO is used to carry out controller parameter intelligent optimization for the two APF-ATRUs.

The target of optimization is to minimize DC voltage tracking error and harmonic current simultaneously. Thus, the following multi-objective performance indexes (20) are chosen, which are the ITAE performance index and the THD performance index. Because an APF-ATRU is composed of two independent rectifier bridges, actual objective functions are averages of two sets of ITAE and THD, respectively. J_{11} and J_{12} are ITAE for the voltage tracking requirement of the two APF-ATRUs, respectively. J_{21} and J_{22} are THD for the harmonic current demand of the two APF-ATRUs, respectively.

$$J_{11} = \int_0^{\infty} t |e_{u_1}(t)| dt \quad (20a)$$

$$J_{12} = \int_0^{\infty} t |e_{u_2}(t)| dt \quad (20b)$$

$$J_{21} = \frac{\sqrt{\sum_{n=2}^{\infty} I_{1sn}^2}}{I_{1s1}} \quad (20c)$$

$$J_{22} = \frac{\sqrt{\sum_{n=2}^{\infty} I_{2sn}^2}}{I_{2s1}} \quad (20d)$$

where e_{u_1} and e_{u_2} are voltage tracking of the two APF-ATRU, respectively. I_{1sn} and I_{2sn} are the effective values of the n -th harmonic current of the two APF-ATRU, respectively. I_{1s1} and I_{2s1} are the effective values of fundamental current of the two APF-ATRU, respectively.

Three parameters, k_{pU} , k_{iU} , and $k_{\lambda U}$, need to be optimized. Therefore, when GWO is used to realize intelligent control for APF-ATRU, the $\vec{X}(t_{GWO})$ described by (13) for each t_{GWO} is $\vec{X} = [k_{pU}, k_{iU}, k_{\lambda U}]$.

4. Virtual Synchronous Generator Based DC/AC Design

Aircraft has different loads in different flight conditions, and there are probably sudden AC loads changes, which cause both AC bus and DC bus fluctuate. These fluctuations are instantaneous. At this time, it is not enough to only control the power supply system in DC-side since there is a time lag in the voltage adjustment process. The preferred way is to have corresponding adjustment means for AC bus as well, so that the MEA electrical power system can keep the DC bus voltage in the case of sudden AC loads changes. Therefore, a suitable control method should be designed for DC/AC inverter.

The DC/AC inverter on a traditional aircraft is the aero static inverter (ASI), whose main function is to convert the electrical energy of a DC power supply into AC power for the use of electrical equipment.

With the development of MEA, the number of airborne equipment is increasing, and the power supply capacity of the power supply system is becoming larger and larger. The traditional ASI can no longer meet the requirements of large power supply capacity. Moreover, the AC power from the ASI cannot achieve closed-loop control, and thus, the voltage amplitude and frequency are susceptible to load changes.

VSG is a new inverter control strategy, which can use the energy storage device to simulate the rotor inertia and damping characteristics of synchronous generator, and improve the operation characteristics of the inverter [34–36]. Compared with the traditional DC/AC inverter control scheme, VSG can simulate the characteristics of synchronous generator active frequency regulation and reactive power voltage regulation through control algorithm, to ensure the stability of the AC bus. At present, VSG is widely studied in micro-grid. Because MEA power system is a kind of independent micro-grid, VSG can be used to aviation field.

Therefore, VSG technology is proposed to adjust the DC/AC inverter in this paper as shown in Figure 2, so as to insure the AC bus has satisfied performance, such as strong stability of bus voltage, current and frequency, and good fault tolerance.

The main circuit topology of DC/AC with VSG control algorithm is shown in Figure 10.

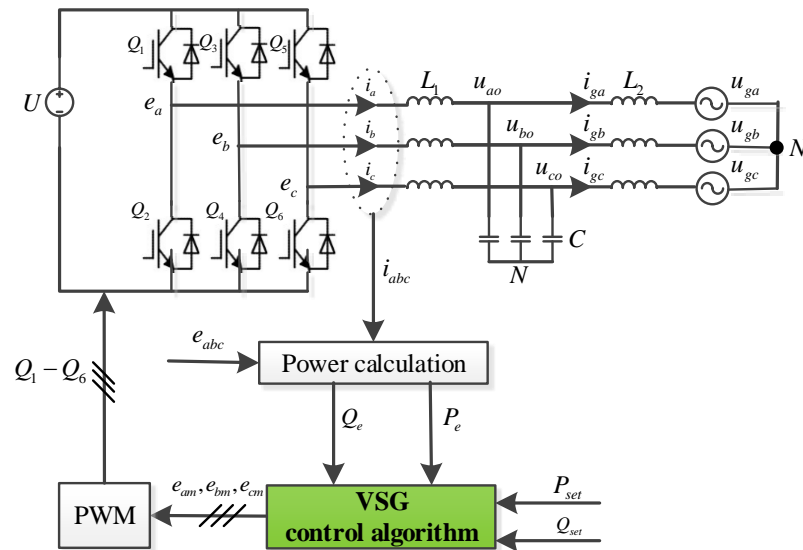


Figure 10. Main circuit topology of DC/AC with VSG control algorithm.

In Figure 10, Q_1 – Q_6 are six switch tubes; the u_{a0}, u_{b0}, u_{c0} are equivalent to the output voltages of synchronous generator; the u_{ga}, u_{gb}, u_{gc} are voltages output to the hybrid power system; L_1, C, L_2 constitutes a filter and the midpoint voltage of the bridge arm (e_a, e_b, e_c) simulates the internal potential of the synchronous generator. The control system consists of power calculation, VSG control algorithm and pulse width modulation (PWM) technology.

The active and reactive power of VSG is calculated as

$$P_e = e_\alpha i_\alpha + e_\beta i_\beta \tag{21a}$$

$$Q_e = e_\beta i_\alpha - e_\alpha i_\beta \tag{21b}$$

where e_α and e_β are obtained by coordinate transformation of e_a, e_b, e_c . Similarly, i_α and i_β are obtained by coordinate transformation of circuit current.

The VSG can simulate the inertia of synchronous generator, and its active frequency modulation characteristics can be expressed by the torque formula of the mechanical part of the generator as

$$T_{set} + D_P(\omega_n - \omega) - T_e = J_P \frac{d\omega}{dt} \tag{22a}$$

$$\theta = \int \omega dt \tag{22b}$$

The characteristics of reactive voltage regulation can be described as

$$Q_{set} + \sqrt{2}D_Q(U_n - U_0) - Q_e = K_Q \frac{d(\sqrt{2}E_m)}{dt} \tag{23}$$

where P_{set} and Q_{set} , respectively, for set point of active power and reactive power. J_P is the moment of inertia of the rotor, T_{set} is on behalf of the mechanical torque given, T_e is the electromagnetic torque, D_P is damping coefficient, θ refers to the rotor angle, ω is for rotor angular velocity, D_Q represents droop coefficient, K_Q represents moment coefficient, U_0 is for output voltage effective value, U_n is rated voltage effective value, and E_m is for modulation wave effective value.

The three-phase modulated wave can be expressed as

$$e_{am} = \sqrt{2}E_m \sin \theta \tag{24a}$$

$$e_{bm} = \sqrt{2}E_m \sin(\theta - \frac{2\pi}{3}) \tag{24b}$$

$$e_{cm} = \sqrt{2}E_m \sin(\theta + \frac{2\pi}{3}) \tag{24c}$$

Figure 11 shows VSG control block diagram. There are two main parts in Figure 11: one is the active power loop, and the other is the reactive power loop. It can be found that the active loop regulates the frequency of the output voltage, and the reactive loop outputs the amplitude of the output voltage.

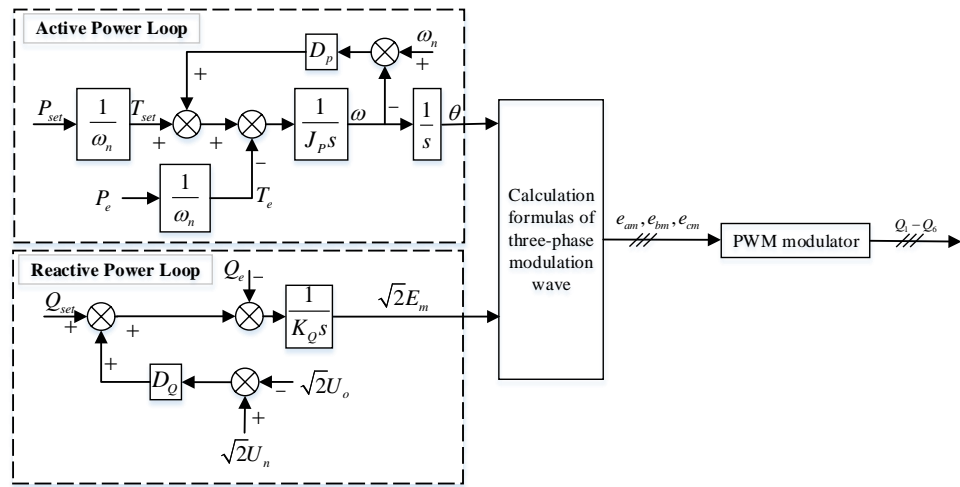


Figure 11. VSG control block diagram.

5. Simulation

The simulation platform of MEA power control system as shown in Figure 12. In Figure 12, the outlets 1, 2, 3, and 4 relate to the performance indexes J_{11} , J_{21} , J_{12} , and J_{22} , respectively.

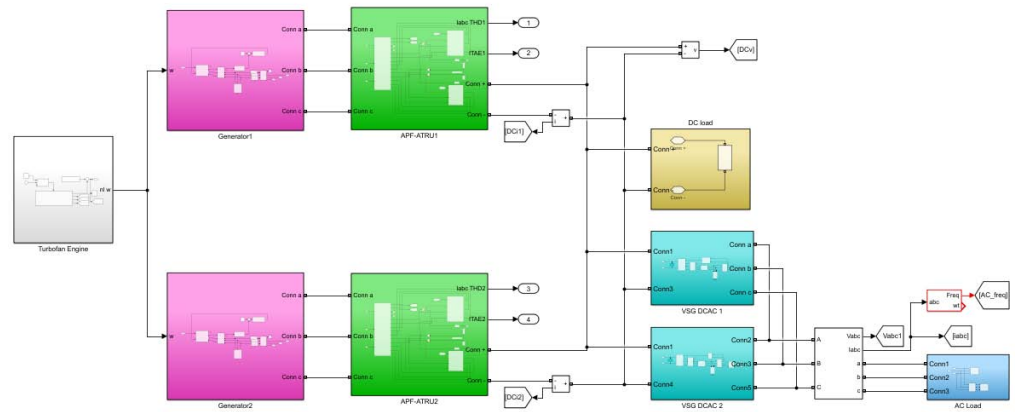


Figure 12. Simulation platform of MEA power control system.

Consider that the dynamic of aircraft engine is much slower than that of AC/DC, the optimization of aircraft engine control law is separated from that of AC/DC in the simulation. After obtaining the optimized aircraft engine intelligent SMFTC law (11) according to Figure 4, the whole MEA power control system is optimized by GWO on the basis of Figure 9.

5.1. Intelligent Fault-Tolerant Control on Aircraft Engine

In this subsection, simulation on a twin-shaft aircraft engine is performed to illustrate the theoretical results proposed in this paper. The linear part of the aircraft engine model used here is adopted from [25].

According to (6), considering (2) and based on [25], here, x , y , u are normalized variables. They are dimensionless, and the units of them are not shown in the following simulation figures in this subsection. The matrices A , B , C , and D are $A = \begin{bmatrix} -2.148 & -0.403 \\ 2.862 & -3.017 \end{bmatrix}$, $B = \begin{bmatrix} 0.298 & 0.594 \\ 0.285 & 1.708 \end{bmatrix}$, $C = \begin{bmatrix} 0 & 1 \\ -0.013 & -0.364 \end{bmatrix}$, $D = \begin{bmatrix} 0 & 0 \\ 0.365 & -0.232 \end{bmatrix}$, respectively. It is supposed that the actuator faults coefficient matrix is $\rho = \text{diag}\{0.8, 0.8\}$. Obviously, the matrix A is Hurwitz, (A, B) is controllable, $B\rho$ is invertible.

It is supposed that the lumped uncertainties occur from the 2nd second. The lumped disturbance $\eta = -0.2 \times Ax - 0.1 \times Bu + \begin{bmatrix} 12x_1^2 - x_2^2 \\ -1.7x_1^2 + x_2^2 \end{bmatrix} + \begin{bmatrix} 0.02\exp(-20(t-2)) \\ -0.01\exp(-10(t-2)) \end{bmatrix}$. Clearly, there are both time-vary disturbance and non-linear term in η . Moreover, it is noted that there exists non-linear cross-channel interaction in η , which indicates the complex dynamics of the aircraft engine.

Assume the initial deviation state vector from operating point is $x(0) = [-0.1, 0.1]^T$. An iteration of GWO optimal result of SMFTC for aircraft engine is given in Figure 13.

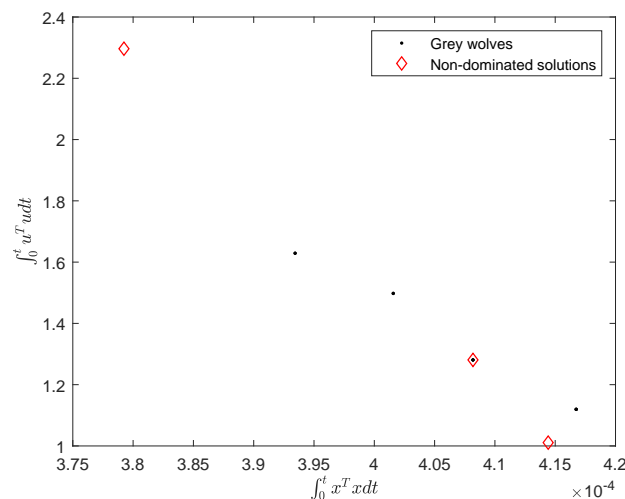


Figure 13. An iteration of GWO optimal result.

Figure 13 illustrates the wolves search preys, and there are three possible positions of preys for dominating. Therefore, users can select a satisfying $\vec{X} = [\sigma_1, \sigma_2, k_1, k_2, q_1, q_2]$ from the three possible positions.

According to Figure 13, if users pay more attention to minimizing inputs consumption, the rightmost non-dominated solution point can be chosen as the optimal point; by contrast, to choose the leftest; or give consideration to both performance indexes, to select the middle one.

Table 1 shows the chosen values of $[\sigma_1, \sigma_2, k_1, k_2, q_1, q_2]$ under SMFTC and Intelligent SMFTC methods, respectively. In Table 1, the parameters in the second row for SMFTC method are tuned by manual work through lots of attempts and can ensure the closed-loop system to be stable. While, because minimizing inputs consumption has attracted more attention in this paper, the parameters in the third row of Table 1 are selected for the Intelligent SMFTC method, after seeking by GWO automatically.

Table 1. Designable parameters in controllers for aircraft engine.

Methods	σ_1	σ_2	k_1	k_2	q_1	q_2
SMFTC	5	5	5	5	5	5
Intelligent SMFTC	4.0829	1.8045	1.3552	2.9426	1.8464	4.1251

Simulation results on aircraft engine are shown in Figures 14–19. The control performance comparison of aircraft engine is illustrated in Table 2.

Table 2. Control performance comparison of aircraft engine.

Methods	$\sum x^T x$	$\sum u^T u$	$ \max(W_{fb}) $	$ \max(A_8) $	$ \max(T_5) $	$ \max(n_h) $	$ \max(n_l) $
SMFTC	3.7849×10^{-4}	2.3379	1.0325	0.2390	0.4288	0.0011	0.0012
Intelligent SMFTC	4.6818×10^{-4}	0.5354	0.4136	0.0909	0.1685	0.0012	0.0011

In Tables 1 and 2 and Figures 14–19, “SMFTC” represents the controller without optimizing, and “Intelligent SMFTC” represents the controller with intelligent optimization by GWO. Figures 14–18 show the comparison of control performance between SMFTC and Intelligent SMFTC, when there is no lumped disturbance. Figure 19 gives the control results of aircraft engine with lumped disturbance since the 2nd second under Intelligent SMFTC method.

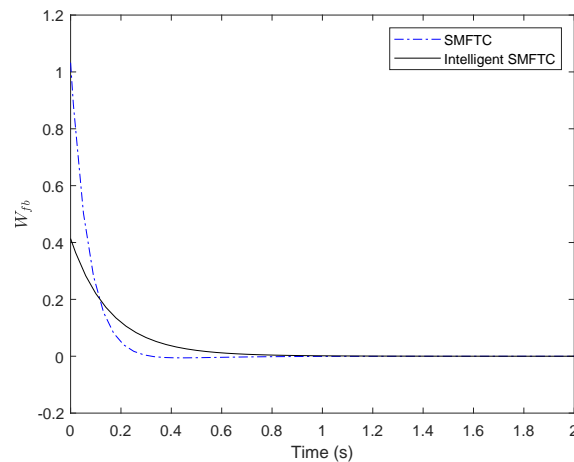


Figure 14. Normalized deviation of fuel flow ratio.

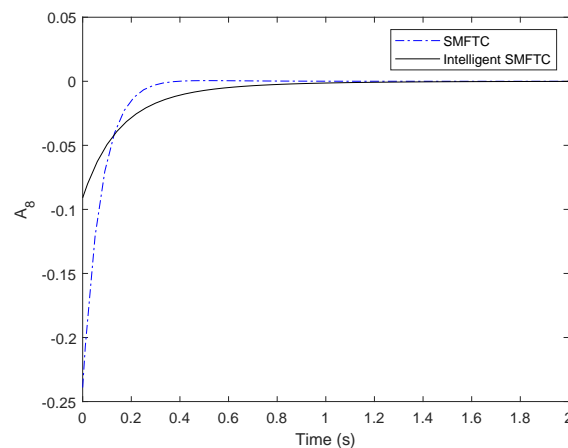


Figure 15. Normalized deviation of nozzle throat area.

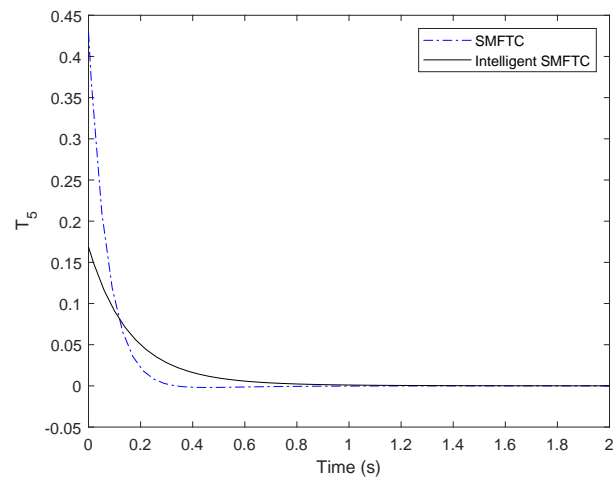


Figure 16. Normalized deviation of total temperature of low-pressure turbine.

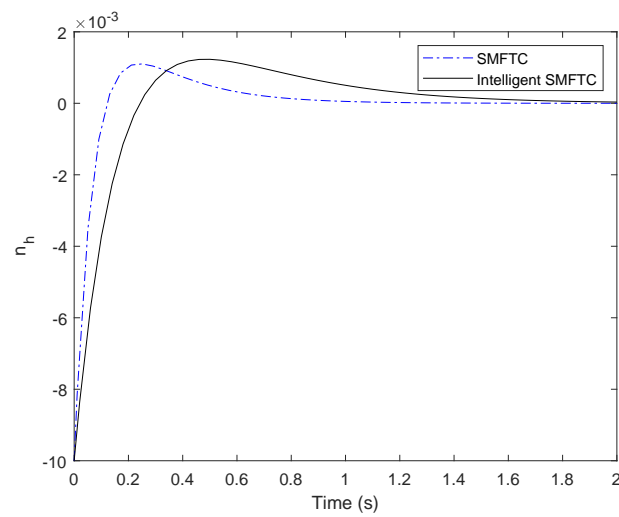


Figure 17. Normalized deviation speed of high-pressure spool.

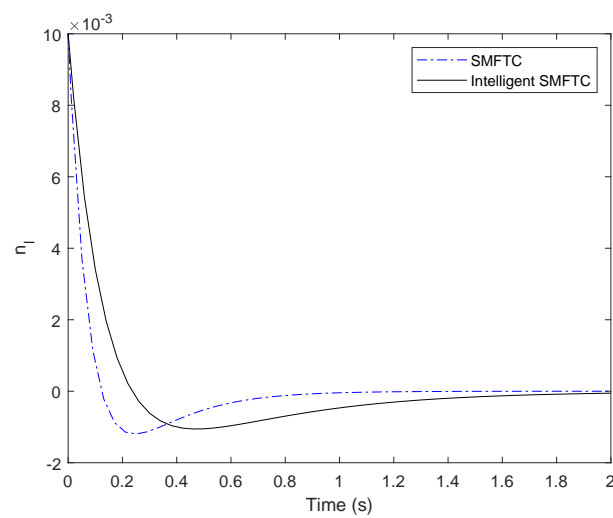


Figure 18. Normalized deviation speed of low-pressure spool.

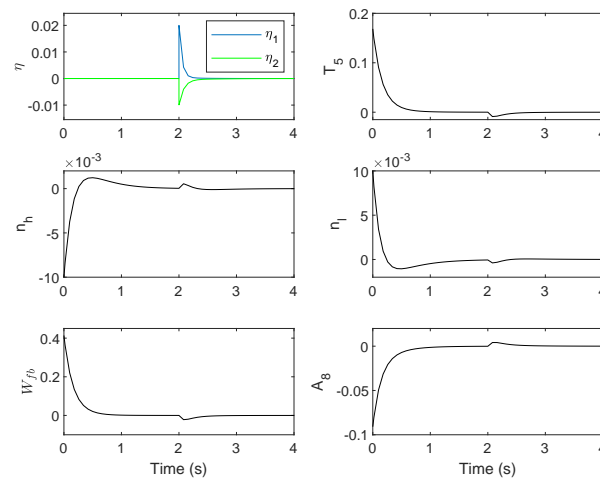


Figure 19. Intelligent SMFTC for aircraft engine with lumped disturbance since 2nd second.

It can be seen from Table 2 and Figures 14–16 that the maximum absolute values of W_{fb} , A_8 and T_5 are decreased significantly under Intelligent SMFTC method.

Figures 17 and 18 show that the maximum absolute values of n_h and n_l are almost the same under the two control methods, with the maximum absolute values of n_l is a bit smaller with Intelligent SMFTC. Because the generators are driven by the low-pressure spool, it is desired that the over-shooting of n_l is small.

As mentioned above, minimizing inputs consumption has attracted more attention than states deviations. Table 2 shows the sum of squared inputs are dropped greatly under Intelligent SMFTC method, the dropping percentage is $\frac{2.3379-0.5354}{2.3379} \times 100\% = 77.10\%$; while the sum of squared states deviations increased as small as 0.8969×10^{-4} , the increasing percentage is $\frac{4.6818-3.7849}{3.7849} \times 100\% = 23.70\%$. Therefore, the optimization by GWO has realized the performance requirements.

As shown in Figures 14–18, dynamic is slower after optimizing, because minimum input consumption is considered, nevertheless, all inputs, outputs and states can be stable in 2 s, which is an acceptable setting time for aircraft engine.

Figure 19 shows the simulation results about intelligent SMFTC for aircraft engine with lumped disturbance since 2nd second. Obviously, all of W_{fb} , A_8 , T_5 , n_h , n_l are affected little by lumped disturbance η , and are back to steady-state quickly.

5.2. Intelligent Control for the Whole MEA Power System

In this subsection, the Intelligent SMFTC for aircraft engine has been applied, and the purpose of this subsection is to determine the optimized designable FOPI parameters in voltage outer loop of APF-ATRU, as shown in Figure 9, and show the simulation results about the intelligent control for the whole MEA power system.

Thus, Figure 20 gives the control effect of DC voltage and current comparison among PI, FOPI and Intelligent FOPI three controllers in 0.7 s, when APF-ATRU are used in the MEA power system. Meanwhile, the lumped disturbance is shown in Figure 21. Figures 22–25 show the control effect of comparison between no APF and has APF in MEA power system for 3.8 s. Considering the similar dynamics of three phases on AC bus, the voltage, current and frequency can be compared on only one phase, as shown in Figures 23–25, respectively.

In order to illustrate the robustness of the MEA power system, it is supposed that:

- An AC load incrementation adds into system during [0.7, 0.8] second. The AC load incrementation is of active power 2000 (W) and inductive reactive power 1000 (positive var). Before 0.7 s, the AC load is of active power 4000 (W) and inductive reactive power 2000 (positive var). Namely, the incrementation is of 50%;

- One of DC/AC inverters failure occurs during [1.4, 1.5] seconds. During this period, the faulty DC/AC inverter is disconnected, and the load power is fully borne by the other DC/AC inverter.
- Lumped disturbance for aircraft engine appears from 1.8 s.

The main parameters of electric components are given in Appendix A.

For the two generators in the MEA power system, the PI controller parameters are chosen as $k_{pG} = 50$, $k_{iG} = 100$. For the two APF-ATRU in the MEA power system, the PI controller parameters for current inner loop are chosen as $k_{pI} = 3$, $k_{iI} = 0.1$. Three controllers are designed for the voltage outer loop of APF-ATRU, and the parameters of each controller is given in Table 3.

Table 3. Parameters in controllers for the voltage outer loop of APF-ATRU.

Methods	k_{pU}	k_{iU}	$k_{\lambda U}$
PI	1	0.1	0
Fractional Order PI (FOPI)	1	0.1	-0.1
Intelligent Fractional Order PI (Intelligent FOPI)	2.1140	0.1047	-0.2340

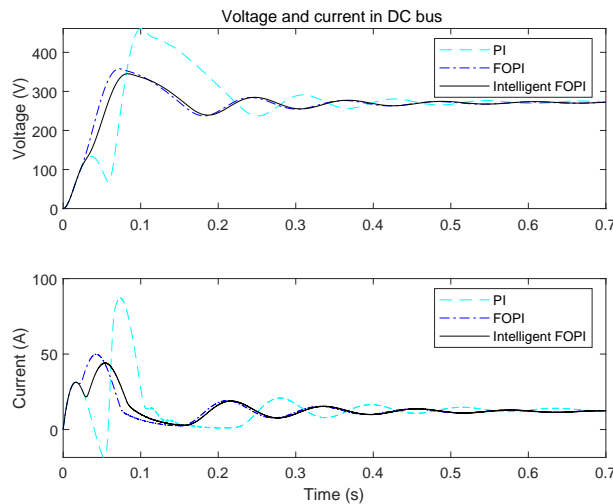


Figure 20. DC voltage and current comparison among three control methods.

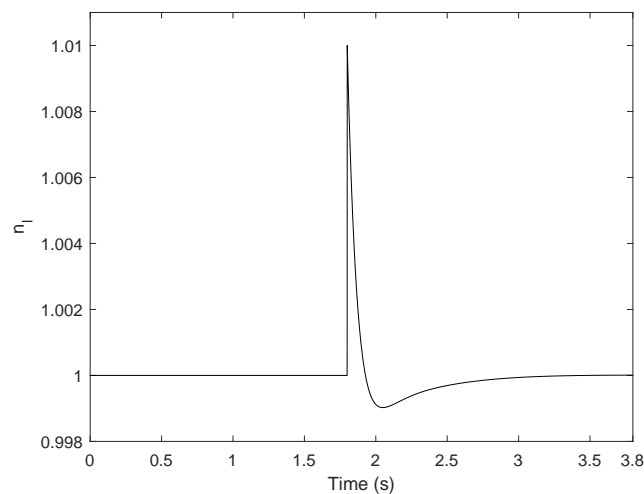


Figure 21. Low-pressure spool speed fluctuation (Case 2).

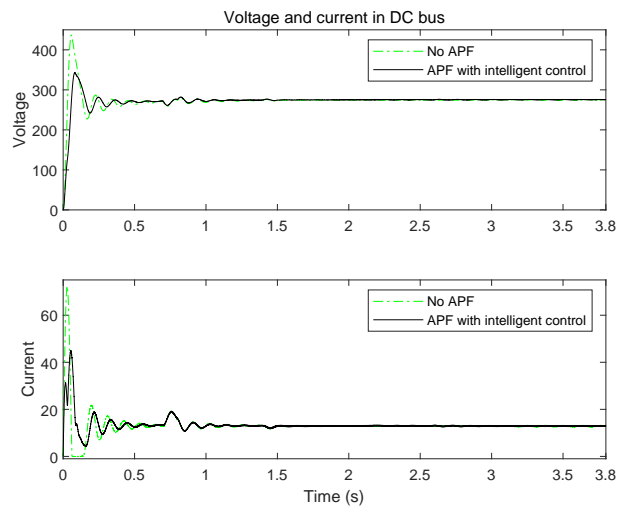


Figure 22. DC voltage and current comparison between no APF and has APF in MEA power system.

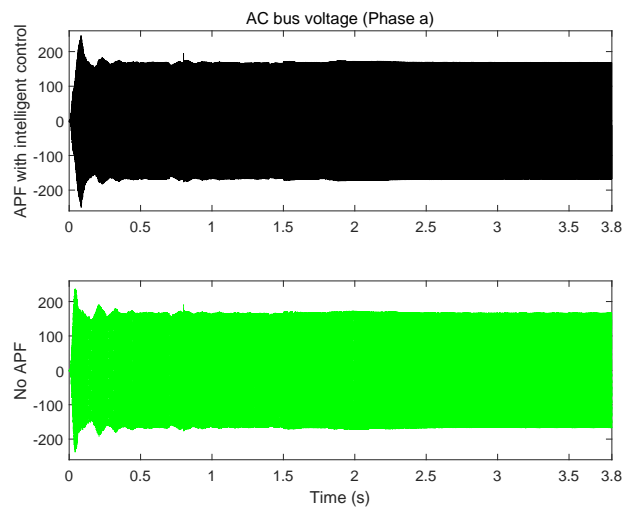


Figure 23. AC bus voltage (Phase a).

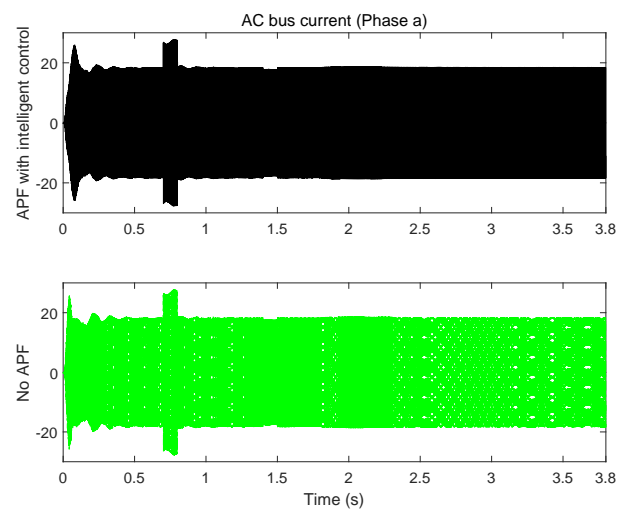


Figure 24. AC bus current (Phase a).

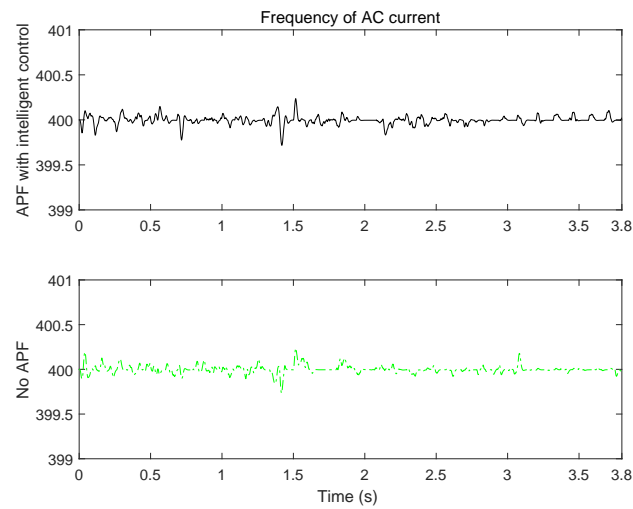


Figure 25. Frequency of AC current.

Obviously, Figure 20 shows that both FOPI and Intelligent FOPI controllers can let the voltage and current in DC bus have better dynamic performance than those under PI controller. The setting time is almost the same under FOPI and Intelligent FOPI controllers. However, the maximal values of overshooting in both voltage and current are the smallest under the control of Intelligent FOPI controller.

Figure 22 shows when the MEA power system does not have APF, the overshooting in DC bus is much greater than that of having APF with intelligent control. The steady-state values of voltage and current in DC bus are 270 V and 13 A, respectively. For the case, there is no APF, the maximum values of voltage is 437.2, and current is 72.11, respectively. The percentages of overshooting are $\frac{437.2-270}{270} \times 100\% = 75.26\%$, $\frac{72.11-13}{13} \times 100\% = 454.69\%$, respectively. For the case, there is APF with intelligent control, the maximum values of voltage is 343.2, and current is 44.85, respectively. The percentages of overshooting are $\frac{343.2-270}{270} \times 100\% = 27.11\%$, $\frac{44.85-13}{13} \times 100\% = 245.00\%$, respectively. Clearly, the maximum value of DC voltage drops almost 50%, and the maximum value of DC current drops almost 200%.

Moreover, it is seen that the AC load incrementation brings some fluctuation for the voltage and current of DC bus; however, the fluctuation disappears in 0.6 s after the AC load incrementation is removed. In addition, DC/AC failure changes the voltage and current of DC bus tiny. Thus, the VSG for DC/AC is effective to guarantee the stability of voltage and current in DC bus.

Although the lumped disturbance makes the low-pressure spool speed of aircraft engine change, the voltage and current of DC bus are affected little.

From Figures 23–25, one can find that the curves of voltage, current, and frequency in AC-side are similar, whether APF is in the MEA system or not. Namely, the performance of the AC-sides is not affected by the APF in the DC-side. Thus, for the AC-side, the VSG is important to ensure the voltage, current, and frequency are of desired performance. Figures 23 and 25 show voltage and frequency in the AC bus are influenced by the AC load incrementation, DC/AC fault and lumped disturbance for aircraft engine little. Obviously, it is shown in Figure 24 that current in the AC bus is increased with the increasing of AC load, and once the AC load incrementation is removed, the current is back to the former level soon.

Therefore, the proposed intelligent control method for the whole MEA power system can guarantee the aircraft engine has strong robustness, fault tolerance to actuator faults, and minimal energy consumption; the voltage and current in DC bus and AC bus have satisfying steady-state and dynamic performance, strong robustness to the sudden change of AC load, DC/AC fault and lumped disturbance happened in aircraft engine; and the frequency of AC current remains around specified value.

6. Conclusions

An intelligent FTC method is presented for a kind of MEA AC/DC hybrid electrical power system in this paper. The main features of this method include:

- A multi-objective optimization Intelligent SMFTC method is proposed for aircraft engine, with fault actuators being considered, to ensure that the states of aircraft engine have strong robustness and fault-tolerance performance.
- Intelligent FOPI controllers are designed for the AC/DC rectifiers, which are 12-pulse ATRU with APF by optimizing multiple performance indexes, so as to reduce the fluctuation in the DC bus voltage.
- VSG method is applied for DC/AC inverters, in order to realize that the AC-side has satisfying voltage, current, and frequency, no matter the sudden change of AC load happens or DC/AC fault occurs.

The MEA power system is considered as a holistic system, which is comprised of an aircraft engine, two electric generators, two AC/DC rectifiers, two DC/AC inverters, DC loads, and AC loads.

Simulation results verify the proposed intelligent FTC method can guarantee the whole MEA hybrid AC/DC power system has satisfying performance, such as high steady-state and dynamic performance, strong robustness, and fault tolerance.

Since the proposed method has shown high efficiency, it is advisable to consider their application to other possible MEA hybrid power systems or their components, for example, electric drives.

Author Contributions: Conceptualization, L.X.; methodology, R.R.S.; validation, Peisong Liu; software, C.L.; investigation, L.X.; writing—original draft preparation, L.X.; writing—review and editing, P.L. All authors have read and agreed to the published version of the manuscript.

Funding: This research was funded by the National Natural Science Foundation of China grant number 51876089.

Institutional Review Board Statement: Not applicable.

Informed Consent Statement: Not applicable.

Data Availability Statement: Not applicable.

Acknowledgments: The authors would like to acknowledge all of team-mates.

Conflicts of Interest: The authors declare no conflict of interest.

Appendix A

Appendix A.1. Generator Parameters

Implements a three-phase simplified synchronous machine. Machine is modeled as an internal voltage behind a R-L impedance. Stator windings are connected in wye to an internal neutral point.

- (1) Nominal power, line-to-line voltage, and frequency [Pn(VA), Vn(Vrms), fn(Hz)]: $[90 \times 10^3, 115 \times \sqrt{3}, 400]$.
- (2) Internal impedance [R(ohm), L(H)]: $[0.0204, 0.8104 \times 10^{-3}]$.

Appendix A.2. ATRU Parameters

Appendix A.2.1. Three Windings Linear Transformer

- (1) Nominal power and frequency [Pn(VA), fn(Hz)]: $[250 \times 10^6, 400]$.
- (2) Winding 1 parameters [V1(Vrms), R1(ohm), L1(H)]: $[100, 0, 0]$.
- (3) Winding 2 parameters [V2(Vrms), R2(ohm), L2(H)]: $[18, 0, 0]$.
- (4) Winding 3 parameters [V3(Vrms), R3(ohm), L3(H)]: $[18, 0, 0]$.

Appendix A.2.2. Universal Bridge

Power Electronic device: Diodes; Number of bridge arms: 3; Snubber resistance R_s (Ohms): 1×10^5 ; Snubber capacitance C_s (F): inf; R_{on} (Ohms): 1×10^{-3} ; $L_{on}(H)$: 0; Forward voltage V_f (V): 0.

Appendix A.3. APF Parameters

Switch controlled by a gate signal in parallel with a series RC snubber circuit. Internal resistance R_{on} (Ohms): 0.001; Initial state (0 for 'open', 1 for 'closed'): 0; Snubber resistance R_s (Ohms): 1×10^5 ; Snubber capacitance C_s (F): inf.

Appendix A.4. DC/AC Inverter Parameters

Power Electronic device: IGBT/Diodes; Number of bridge arms: 3; Snubber resistance R_s (Ohms): 1×10^6 ; Snubber capacitance C_s (F): inf; R_{on} (Ohms): 1×10^{-4} .

Appendix A.5. VSG Parameters

$P_{set} = 8000$, $J_p = 0.057$, $D_p = 2000$, $w_n = 2\pi \times 400$, $Q_{set} = 4000$, $K_Q = 20,000$, $D_Q = 0.00025$, $U_n = 115$.

Appendix A.6. AC Load

Nominal phase-to-phase voltage V_n (Vrms): $115\sqrt{3}$; Nominal frequency f_n (Hz): 400; Active power P (W): 4000; Inductive reactive power Q_L (positive var): 2000.

Appendix A.7. DC Load

Branch type: RL; Resistance (Ohms): 50; Inductance (H): 1×10^{-3} .

References

1. Wheeler, P. Technology for the more and all electric aircraft of the future. In Proceedings of the 2016 IEEE International Conference on Automatica (ICA-ACCA), Curico, Chile, 19–21 October 2016, pp. 1–5.
2. Quigley, R.E. More Electric Aircraft. In Proceedings of the Eighth Annual Applied Power Electronics Conference and Exposition, San Diego, CA, USA, 7–11 March 1993; pp. 906–911.
3. Xu, K.L.; Xie, N.; Wang, C.M.; Deng, J.W. Static Modeling and Power Flow of the More Electric Aircraft Power System. In Proceedings of the 2016 3rd International Conference on Systems and Informatics (ICSAI 2016), Shanghai, China, 19–21 November 2016; pp. 193–198.
4. Karimi, K.J. *Future Aircraft Power Systems-Integration Challenges*; Technical Report; The Boeing Company: Chicago, IL, USA, 2007.
5. Sarlioglu, B.; Morris, C. More Electric Aircraft: Review, Challenges, and Opportunities for Commercial Transport Aircraft. *IEEE Trans. Transp. Electrification* **2015**, *1*, 54–64. [[CrossRef](#)]
6. Cheng, L.; Zhang, F.; Liu, S.; Zhang, Z. Configuration Method of Hybrid Energy Storage System for High Power Density in More Electric Aircraft. *J. Power Sources* **2020**, *445*, 227322. [[CrossRef](#)]
7. Oyori, H.; Morioka, N. Integrated Power Management System for the More Electric Aircraft. In Proceedings of the 51st AIAA Aerospace Sciences Meeting Including the New Horizons Forum and Aerospace Exposition, AIAA 2013-1071, Grapevine, TX, USA, 7–10 January 2013; pp. 1–7.
8. Dunham, W.; Hency, B.; Kolmanovsky, I.; Girard, A. Predictive Propulsion and Power Control for Large Transient Power Loads in a More Electric Aircraft. In Proceedings of the 2017 American Control Conference (ACC), Seattle, WA, USA, 24–26 May 2017; pp. 4055–4061.
9. Xiao, L.; Xu, M.; Chen, Y.; Chen, Y. Hybrid Grey Wolf Optimization Nonlinear Model Predictive Control for Aircraft Engines Based on an Elastic BP Neural Network. *Appl. Sci.* **2019**, *9*, 1254. [[CrossRef](#)]
10. Xiao, L.; Meng, Z.; Huang, X.; Ma, L. Adaptive Observer based Fault Tolerant Control for Aircraft Engine with Sensors and Actuators Faults. In Proceedings of the 2019 Chinese Control Conference (CCC), Guangzhou, China, 27–30 July 2019; pp. 4885–4889.
11. Jiao, N.; Liu, W.; Meng, T.; Sun, C.; Jiang, Y. Decoupling Start Control Method for Aircraft Wound-rotor Synchronous Starter-generator Based on Main Field Current Estimation. *IET Electr. Power Appl.* **2019**, *13*, 863–870. [[CrossRef](#)]
12. Lin, C.; Xiao, L.; Sattarov, R. Power System Control of More-electric Aircraft Engine Based on Double Closed Loop Feedback. In Proceedings of the 2019 International Conference on Electrotechnical Complexes and Systems (ICOECS), Ufa, Russia, 22–25 October 2019; pp. 1–6.

13. Zadeh, M.K.; Gavagsaz-Ghoachani, R.; Nahid-Mobarakeh, B.; Pierfederici, S.; Molinas, M. Stability analysis of hybrid AC/DC power systems for more electric aircraft. In Proceedings of the 2016 IEEE Applied Power Electronics Conference and Exposition (APEC), Long Beach, CA, USA, 20–24 March 2016; pp. 446–452.
14. Cavallo, A.; Canciello, G.; Russo, A. Integrated Supervised Adaptive Control for the More Electric Aircraft aircraft. *Automatica* **2020**, *117*, 108956. [[CrossRef](#)]
15. Canciello, G.; Cavallo, A.; Schiavo, A.L.; Russo, A. Multi-objective Adaptive Sliding Manifold Control for More Electric Aircraft. *ISA Trans.* **2020**, *107*, 316–328. [[CrossRef](#)] [[PubMed](#)]
16. Buticchi, G.; Bozhko, S.; Liserre, M.; Wheeler, P.; Al-Haddad, K. On-board Microgrids for the More Electric Aircraft Technology review. *IEEE Trans. Ind. Electron.* **2018**, *66*, 5588–5599. [[CrossRef](#)]
17. Roberts, R.A.; Donovan, A.; Nuzum, S.R.; Wolff, M. Impact of High Energy Pulsed Systems on an Aircraft’s Power and Thermal Management System. In Proceedings of the 57th AIAA/ASCE/AHS/ASC Structures, Structural Dynamics, and Materials Conference, San Diego, CA, USA, 4–8 January 2016; p. 0672.
18. Alsmadi, Y.M.; Utkin, V.; Haj-Ahmed, M.; Xu, L.; Abdelaziz, A.Y. Sliding-mode Control of Power Converters: AC/DC Converters & DC/AC Inverters. *Int. J. Control* **2018**, *91*, 2573–2587.
19. Aboushal, M.; Moustafa, M.M.Z. A New Unified Control Strategy for Inverter-based Micro-grid Using Hybrid Droop Scheme. *Alex. Eng. J.* **2019**, *58*, 1229–1245. [[CrossRef](#)]
20. Liu, J.; Miura, Y.; Bevrani, H.; Ise, T. Enhanced Virtual Synchronous Generator Control for Parallel Inverters in Microgrids. *IEEE Trans. Smart Grid* **2016**, *8*, 2268–2277. [[CrossRef](#)]
21. Mirjalili, S.; Mohammad, S.; Lewis, A. Grey Wolf Optimizer. *Adv. Eng. Softw.* **2014**, *69*, 46–61. [[CrossRef](#)]
22. Zahedi, F.; Zahedi, Z. A Review of Neuro-Fuzzy Systems Based on Intelligent Control. *arXiv* **2018**, arXiv:1805.03138.
23. Barzegar, A.; Su, R.; Wen, C.; Rajabpour, L.; Zhang, Y.; Gupta, A.; Gajanayake, C.; Lee, M.Y. Intelligent Power Allocation and Load Management of More Electric Aircraft. In Proceedings of the 2015 IEEE 11th International Conference on Power Electronics and Drive Systems, Sydney, Australia, 9–12 June 2015; pp. 533–538.
24. Khalid, S. Performance Evaluation of Adaptive Tabu Search and Genetic Algorithm Optimized Shunt Active Power Filter Using Neural Network Control for Aircraft Power Utility of 400 Hz. *J. Electr. Syst. Inf. Technol.* **2018**, *5*, 723–734. [[CrossRef](#)]
25. Xiao, L.; Du, Y.; Hu, J.; Jiang, B. Sliding Mode Fault Tolerant Control with Adaptive Diagnosis for Aircraft Engines. *Int. J. Turbo Jet-Engines* **2018**, *35*, 49–57. [[CrossRef](#)]
26. Nasiri, A.; Nguang, S.K.; Swain, A.; Almkhles, D. Passive Actuator Fault Tolerant Control for a Class of MIMO Nonlinear Systems with Uncertainties. *Int. J. Control* **2019**, *92*, 693–704. [[CrossRef](#)]
27. Zhang, Y.; Peng, G.O.H.; Banda, J.K.; Dasgupta, S.; Husband, M.; Su, R.; Wen, C. An Energy Efficient Power Management Solution for a Fault-tolerant More Electric Engine/ Aircraft. *IEEE Trans. Ind. Electron.* **2018**, *66*, 5663–5675. [[CrossRef](#)]
28. Wheeler, P.; Bozhko, S. The More Electric Aircraft Technology and challenges. *IEEE Electr. Mag.* **2014**, *2*, 6–12. [[CrossRef](#)]
29. Yu, X.; Jiang, J. A Survey of Fault-tolerant Controllers Based on Safety-related Issues. *Annu. Rev. Control* **2015**, *39*, 46–57. [[CrossRef](#)]
30. Cooper, J.E. Integrated Strategy for Commercial Aircraft Fault-Tolerant Control. *J. Guid. Control Dyn.* **2018**, *41*, 1419–1430.
31. Huang, J.; Zhang, T.; Ye, Z.; Zhou, W.; Pan, M. *Modern Aviation Power Plant Control*, 3rd ed.; Aviation Industry Press: Highland Park, IL, USA, 2018.
32. Rasmussen, H. *Advanced Control of Turbofan Engines*; Springer: Berlin/Heidelberg, Germany, 2012.
33. Gao, W. *Variable Structure Control Theory and Design Method*; Science Publishing House: New York, NY, USA, 1996.
34. Wu, H.; Ruan, X.; Yang, D.; Chen, X.; Zhao, W.; Lv, Z.; Zhong, Q.C. Small-signal Modeling and Parameters Design for Virtual Synchronous Generators. *IEEE Trans. Ind. Electron.* **2016**, *63*, 4292–4303. [[CrossRef](#)]
35. Li, P.; Hu, W.; Xu, X.; Huang, Q.; Liu, Z.; Chen, Z. A Frequency Control Strategy of Electric Vehicles in Microgrid using Virtual Synchronous Generator Control. *Energy* **2019**, *189*, 116389. [[CrossRef](#)]
36. Cheema, K.M. A Comprehensive Review of Virtual Synchronous Generator. *Electr. Power Energy Syst.* **2020**, *120*, 106006. [[CrossRef](#)]